Department of Construction Sciences
Solid Mechanics

ISRN LUTFD2/TFHF-24/5262-SE(1-42)

Macroscale crease models calibrated to synthetic crease experiments

Master's Dissertation by

Kristján Tómasson

Supervisors:
Mathias Wallin, Prof. Division of Solid Mechanics
Johan Tryding, Adj. Prof. Division of Solid Mechanics and Tetra Pak

Examiner:
Matti Ristinmaa, Prof. Division of Solid Mechanics

Printed by Media-Tryck AB, Lund, Sweden
For information, address:
Division of Solid Mechanics, Lund University, Box 118, SE-221 00 Lund, Sweden
Webpage: www.solid.lth.se

Abstract

This master's thesis presents a method for approximating the folding behavior of paperboard using macroscopic data. Synthetic data is generated by conducting finite element analysis on paperboard modeled using continuum elements and an advanced constitutive law formulated within a thermodynamic framework. The paperboard model undergoes creasing followed by various folding sequences, enabling the extraction of curves that relate bending resistance to a corresponding fold angle. Additionally, a compression test is conducted, and its results are compared with experimental data found in literature. Subsequently an investigation of capturing the synthetic folding behavior is performed, which involves approximating paperboard with beam elements using a fully linear-elastic material model. A single beam element is used to represent the crease, modified to include plasticity modeling, aiming to replicate behavior seen in synthetic data. A parametric study is conducted by introducing parameters concerning the crease beam's geometric attributes, as well as the linear-elastic and plastic material properties of the crease beam. It is found that the initial sequences of folding are captured relatively well, while for folds of increased complexity the ability of the beam to mimic the macroscopic synthetic data deteriorates. The model's limitations are discussed, particularly regarding the possible need to differentiate the crease beam's behavior under monotonic axial loading from pure bending modes, particularly given the method of plasticity modeling employed.

Preface

The work on this thesis began in November of 2023, and has been quite the learning experience, not only related to the work presented, but also on a personal level. At times I could relate to Sisyphus, forever rolling a boulder up a hill, though in general it has been a pleasure. This work also marks the end of six years studying at LTH, years that will be remembered fondly as my journey through life continues.

First and foremost I'd like to thank my supervisors Johan Tryding and Mathias Wallin for their guidance, feedback, insights, and constant encouragement throughout the course of this work. I also express my appreciation to Filip Claesson and Kristofer Robertson for their insightful comments, and technical assistance. Special thanks to Matti Ristinmaa for engaging discussions which helped shape the path that this work took.

Lastly, I am deeply thankful to my friends and family for their support throughout, helping me take my mind off things and simply enjoy the moment.

June 2024
Vildanden, Lund

Jag tillägnar detta arbete till min älskade mamma Hrafnhildur, som ständigt är med mig i hjärta och själ. Jag vet hur stolt du hade varit i denna stund, uppmuntrande och omtänksam som du var. Alltid saknad, aldrig glömd.

Contents

1 Introduction

Paperboard is an essential material for consumer goods packaging. The carton packages produced by Tetra Pak consists of multiple material types, such as polymers, aluminum and paperboard, which is formed into a laminate. A carton produced by Tetra Pak consists on average of 70% by weight of paperboard, providing the main structural rigidity of the finished package.[1] Making consumer goods packages out of raw materials involves a converting process, in which sheets of packaging material are among other operations mechanically deformed, transforming the sheet laminate into a desired geometric configuration.

Paperboard as a material is highly anisotropic, a natural consequence of the paperboard manufacturing process, resulting in a sheet constituted by layers of pulp fibers. Three distinct material directions are used to characterize the behavior of paperboard, the Machine- and Cross-directions, along with the Z-direction, denoted MD, CD and ZD respectively. MD and CD are the directions in-plane, while ZD is the direction perpendicular to the sheet plane. The machine direction is the direction which the pulp fibers of the material are highly aligned on average, as opposed to the cross direction which the pulp fibers are less aligned on average. The out-of-plane Z-direction contains the different paperboard fiber layers, which are bound together by some form of adhesion. [2][3] MD stiffness is typically larger than CD stiffness by a factor 1 to 5, and approximately 100 times larger than ZD stiffness. In the elastic regime paperboard is usually approximated as orthotropic.[4]

A key to converting raw materials into a desired geometry is the material's inelastic properties, the residual plastic strains, damage and cracks after converting operations determines the resulting geometric structure. One of the operations used is folding, which done along predetermined fold lines and fold angles enables a planar sheet to transform into an enclosed package. Ensuring adherence to specified geometrical requirements, meeting qualitative standards for the final product, and minimizing the occurrence of defects are essential aspects in the manufacturing process. In the context of paperboard converting operations, it is customary to crease the paperboard to enhance control over its behavior during folding.

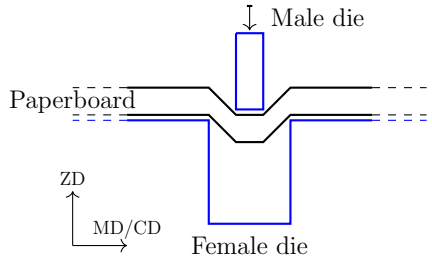

(a) Creasing performed by deforming a paperboard sheet in the out-of-plane direction.

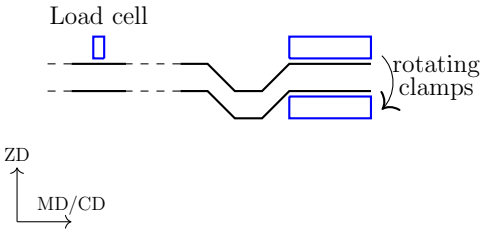

(b) Folding along the crease line by use of rotating clamps and measuring load cell.

Figure 1: Schematic of creasing and subsequent folding of creased paperboard such as in [5]

Creasing introduces local inelastic deformations and subsequent damage to the converting material by pressing a sheet of material between a male and female die set, as depicted in Figure 1a. This procedure plays a pivotal role in mitigating the risk of cracks forming during folding, the prevention of cracks being essential not only for ensuring structural rigidity but also for maintaining aesthetic appeal. Despite its widespread application, scientific understanding of the effects of creasing on the constitutive behavior of paperboard has historically been limited.

Integral to the design of a converting process is the ability to predict the effects that mechanical operations such as creasing and folding have on the material being converted. Gathering and analyzing experimental data lays the foundation for the theoretical models and methods such as the finite element method which is used in order to mimic both observed behavior, but also try to predict behavior that is hard to experimentally measure.

From an experimental standpoint, effort has been put into studying creased paperboard response for simple folds, i.e folding of angle θ from 0 to typically 90° in the "natural" folding direction, while a load cell measures the force response. Results produced by Nagasawa et al. [5] show that the measured bending moment resistance of the creased paperboard specimens are reduced in comparison to the noncreased control specimen, and a relation can be found between creasing depth and the reduction in stiffness. The schematics of the test rig used by Nagasawa et al. [5] is reoccurring in the scientific literature in the context of real physical experiments but also in simulations, where it is used to calibrate and/or verify virtual models. As of this date, the scientific literature lacks experimental data concerning "counter" crease folds, as highlighted by Giampieri [6], illustrated in Figure 2. Furthermore no experimental data exists for paperboard subjected to complex folding, which in this thesis is defined as folds of a crease for a set sequence of angles $[0, \theta_1, \theta_2, \ldots, \theta_n]$, $\theta_{i-1} \neq \theta_i$. Understanding the response of creases subject to complex folds is crucial because it provides valuable insights into the material's behavior. This knowledge is essential for optimizing the converting process, leading to more efficient and effective product design and manufacturing.

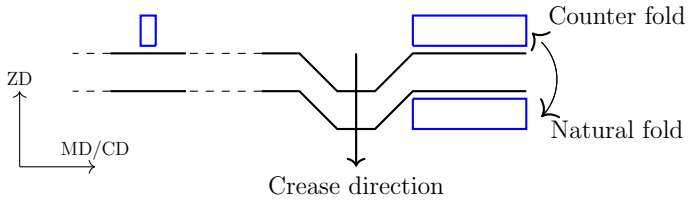

Figure 2: Natural folds result in the indented side, formed by the crease, facing outward in the resulting corner, while counter folds result in the outdented side, formed by the crease, facing outward in the resulting corner.

In the realm of modeling, effort has also been spent in order to mimic creased paperboard behavior. The continued development of a particular material constitutive

model, fundamental to the work of this thesis, is the result of work spanning 20 years [7][8][9][10]. Used in conjunction continuum elements, it has shown promising results in high resolution simulations.

1.1 Super Elements

The use of continuum elements and intricate constitutive laws, especially in the creased zones, necessitates high resolution of the domain. Expanding the scope of the simulation from two-dimensional into three-dimensional space, such as in converting simulations, would drastically increase the number of elements needed in the creased domain, often resulting in computational costs (and time) that is unfeasible. A solution to this problem is the use of *super elements*, which are based on observed macroscopic behavior and can replace computationally expensive parts of the domain in numerical analysis.

A classical example is modeling a coil spring with a spring element and Hooke's law: $F = k \cdot \Delta L$ where k is a constant derived from the macroscopic force response F for a given elongation of ΔL. Super elements have been used in the literature to analyze different collision scenarios between ships [11], model walls with openings and their effect on building structures' response to seismic loads [12], and analyze the response of airplane wings subject to aerodynamic loads [13].

In the given examples, detailed information regarding the stress and strain fields of the domain is not of interest. Instead, the focus is on essential characteristics such as resultant forces and displacements, modeled using macroscopic data. This approach allows for the study of the domain's interaction with the rest of the model. The particularities of the actual deformation that occurs, for example in a crease subjected to folding, are not important as long as the same force response can be obtained. Ideally, a spring element is used to define a force or torque response based on relative nodal displacements or rotations. Alternatively, computationally efficient structural elements such as beam or shell elements can be used.

1.2 Objective

The paperboard material model proposed by Borgqvist et al. [8][9] is used in order to conduct virtual creasing of paperboard, followed by different folding sequences. The macroscopic response extracted from the synthetic data is studied and utilized in order to approximate folding of creased paperboard by use of a beam element. The simulations are performed using Abaqus Standard, a commercial finite element simulation software.

1.3 Limitations

This thesis examines the folding of creased paperboard as a two-dimensional problem by focusing on folds in a single panel along its Machine Direction (MD). However,

in practical applications such as the converting process a three-dimensional object is formed, containing multiple folds across both MD and CD, as well as intermediate directions. Simulations of the full converting process are typically done in three dimensional space. The work is also limited to the study to analyzing the response of single-ply of a board that is in fact multi-ply board. Finally while the constitutive model found in [10] is the most recent model available for use at Tetra Pak, the model found in [9] was used instead, as it was deemed to be more numerically stable. Therefore, this thesis should be viewed as a conceptual study, a proposed modeling and calibration method that can be adapted for newer models or experimental data.

1.4 Structure

The contents of this thesis is essentially comprised of five main sections, the second section containing a description of some modeling methods used in conjunction with finite element analysis to predict paperboard behavior. The third section describes the method used to extract synthetic data in this thesis, along with a detailed description of the load cases that are to be studied virtually, the synthetic results are presented along with an analysis. The fourth section begins with a description of a beam formulation modeled in order to recreate the synthetic data from the previous section. The fifth section is dedicated to results from the beam modeling along with analysis. The final two sections consist of conclusions and recommendations for further work along the same modeling approach.

2 Literature Review of Paperboard Simulations

This section summarizes the literature that exists regarding the continuum scale constitutive modeling of paperboard. A review is also presented of the structural element formulations that have been used in order to model creases, followed by comments regarding applicability of the models for use in converting simulations.

2.1 Constitutive Models

Mäkelä and Östlund [14] formulated an in-plane constitutive model based on the small strain assumption. An orthotropic linear elastic model was used, while inelastic behavior was defined by a non-quadratic yield surface, an associated flow rule and isotropic hardening. The amount of calibration parameters are kept relatively low by adopting the concept of isotropic plasticity equivalent (IPE) material which was introduced by Karafillis and Boyce [15], and modified it to incorporate J_2-flow theory.

Xia [7] implemented a constitutive law based on finite strain theory, which utilized orthotropic linear model for the elastic response. The formulation includes a model for in-plane inelastic behavior by the use of an anisotropic yield surface consisting of six sub-surfaces, implemented by the use of a switch function. Combined with an associated flow rule, the sub-surfaces are able to expand independently of each other.

Harrysson and Ristinmaa [16] formulated a model based on principles of thermodynamics and finite strain theory. An orthotropic, hyper-elastic model was combined with an in-plane inelastic model, treating the out-of-plane behavior as fully elastic. A modified Tsai-Wu criterion was used to distinguish between plastic yield points in tension and compression, along with the use of a non-associated flow rule, enabling the yield surface expansion to be dependent on the mode of yielding.

Inelastic out-of-plane models have been implemented in the form of material constitutive laws, as done by Stenberg [17], but also through the use of interface elements. Xia [7] modeled out-of-plane inelastic behavior by implementing an interface model, intended to capture the occurrence of delamination from the creasing of paperboard. To incorporate both in-plane and out-of-plane models, Xia [7] modeled paperboard as multiple layers of continuum elements, through the out-of-plane direction. These layers contain an in-plane constitutive model with purely elastic behavior in the out-of-plane direction, and interface connections between the continuum element layers to represent out-of-plane inelasticity.

Borgqvist et al. [8][9] built on the work of Xia by reformulating the constitutive laws in a framework that adheres to the principles of thermodynamics. The out-of-plane inelastic behavior was incorporated with the in-plane constitutive model, though the in- and out-of-plane inelastic behavior was still modeled as decoupled. The model is able to capture the effects of creasing, mainly the inelastic deformations during the creasing operation, but also mimic the initial response of folding the creased board, though for

folding of larger degrees the response of the paperboard fold stiffness is overestimated.

Finally Robertsson et al. [10] further built on the model proposed by Borgqvist et al. by including damage, modeling the subsequent weakening of paperboard subject to folding, further increasing the accuracy of the model with respect to the existing experimental data, such as improvements related to mimicking the response of creased paperboard for large degrees of folding, where the Borgqvist model would overestimate the force response, cf. [10, Figure 4]

The virtual paperboard models formulated by Xia, Borgqvist and Robertsson are all tailored for use in conjunction with a continuum element domain, and have all been tested in simulations replicating creasing but also folding, in a similar procedure as that found in [5]. The accuracy of these high resolution models in relation to capturing both creasing and folding experimental data has improved over time, to an extent that it might be possible to use the models in order to predict the behavior of creases subject to more complex loading situations as described earlier.

2.2 Structural Elements

Structural elements, among which are the spring-, bar-, beam- and plate elements, are a family of elements with associated kinematic assumptions that simplify finite element analysis problems. The potential computational cost saved by using structural elements as opposed to continuum elements is certainly beneficial in already costly simulation environments, given that the approximation is done appropriately and yields sufficiently correct results.

Previous attempts of using structural elements for crease representations have been made, a spring-element approach is used by Beldie [18] and Zhao et al. [19], Beldie used a two node element which gives off a force- or moment response related to the relative displacement or rotation of the respective nodal degrees of freedom. Zhao et al. utilized one dimensional torsion springs by using the built in Abaqus feature of rigid hinge connections between two nodes, only allowing for relative rotations in one degree of freedom. Both models were implemented by approximating the crease line as a series of discrete spring elements connecting two paperboard domains modeled using shell elements. The spring element implementations mentioned were used with success when applied to their respective engineering problems, though both models suffer from possible drawbacks. The model by Beldie doesn't contain a local coordinate system, which limits the use of the model to simulations where the element is aligned with the global coordinate system. The model proposed by Zhao et al.could be overly rigid in situations where folding isn't the main deformation mode, such as a crease subjected to compression.

The bar- and hinge formulation introduced by Schenk and Guest [20] utilizes a truss framework on which further kinematic constraints have been formulated which relates

relative rotations of truss sections connected by shared nodes. Violations of the rotational constraint gives rise to an error which is penalized with a stiffness parameter. Since its introduction the bar- and hinge formulation has been expanded upon to include more complex behavior (see for example [21]), though issues could arise in regards to comparability when interfacing shell elements with the truss framework. Bar elements only transfer forces in the direction of its length, a consequence of which is that any bending moment applied to a bar (such as by a neighboring shell element subject to bending) won't be accounted for in analysis. To get around this issue kinematic constraints of some sorts would have to be added between the bar- and shell interface.

Giampieri [6] formulated an interface element to be used specifically in conjunction with neighboring shell elements. Recognizing that the intersecting line of two shell element surfaces can be cast into a third surface, with associated direction vectors that are parallel in the undeformed configuration. Folding around the interface then results in nonparallel direction vectors, forming the basis of the strain measure which used along with an intricate constitutive law, resulting in a model that captures the same crease folding response as that found in the compared experimental data. Likely the most detailed structural element approach, the model hasn't to the author's knowledge been implemented for use in commercial software such as Abaqus, while it is tempting to implement the model it was deemed outside the scope of this thesis due to the sheer complexity of the formulation, opting for a simpler approach.

3 Synthetic Data Acquisition

The simulations required to create synthetic data were performed using Abaqus Standard, based on a version of the model for line-creasing and folding found in [10]. This model assumes a dynamic quasi-static approach, allowing Abaqus to solve the relevant equations using an implicit method. Paperboard was modeled as a single ply material with a thickness t of 0.395 mm, though in reality the paperboard considered is in fact a triple-ply board i.e three different layers constitute the full paperboard laminate, also the thickness t is in itself different from the thickness of the real world physical paperboard. The material parameter data presented in Tables 1 to 3 contain the necessary input data in order to use Borgqvist's model, along with the yield function potential of $k = 3$ [9]:

Elastic parameter	Value
A_1	2267 (MPa)
A_2	279.0 (MPa)
A_3	16.72 (MPa)
A_4	0 (MPa)
A_5	1520 (MPa)
A_6	190.6 (MPa)
A_7	0.0331 (MPa)
A_8	24.1371 (-)

Table 1: Elastic parameters corresponding to table A.2 in [9]

subsurface, ν	Subsurface component, $N_{ij}^{(\nu)}$
1	$N_{11}^{(1)} = 0.9287$, $N_{22}^{(1)} = -0.37091$
2	$N_{11}^{(2)} = -0.2130$, $N_{22}^{(2)} = 0.9770$
3	$N_{12}^{(3)} = 0.7071$
4	$N_{11}^{(4)} = -1$
5	$N_{22}^{(5)} = -1$
6	$N_{12}^{(6)} = -0.7071$
7	$N_{33}^{(7)} = -1$
8	$N_{33}^{(8)} = 1$
9	$N_{33}^{(9)} = 0.7035$, $N_{23}^{(9)} = 0.5025$
10	$N_{33}^{(10)} = 0.7035$, $N_{23}^{(10)} = -0.5025$
11	$N_{33}^{(11)} = 0.7035$, $N_{23}^{(11)} = 0.5025$
12	$N_{33}^{(12)} = 0.7035$, $N_{23}^{(23)} = -0.5025$

Table 2: Subsurface parameters corresponding to table A.1 in [9]

Subsurface, ν	Initial yield, K_0 (MPa)	Hardening, a_ν (MPa)	Hardening, b_ν (-)
1	21.29	26.96	229.021
2	12.88	27.85	26.07
3	13.16	8.742	286.239
4	24.60	-	-
5	16.53	-	-
6	13.16	8.742	286.2
7	0.5	24.37	-
8	0.4280	-	-
9	1.757	-	-
10	1.757	-	-
11	1.757	-	-
12	1.757	-	-

Table 3: Plastic parameters corresponding to table A.3 in [9]

3.1 Creasing

The paperboard was approximated as a two dimensional domain in conjunction with a plane strain assumption was used to model the deformable paperboard segment, with the material constitutive law in [9] implemented as an Abaqus user material. The paperboard segment geometry was modeled by extruding a rectangle with length L of 80 mm, a width W of 38 mm and thickness t of 0.39 mm:

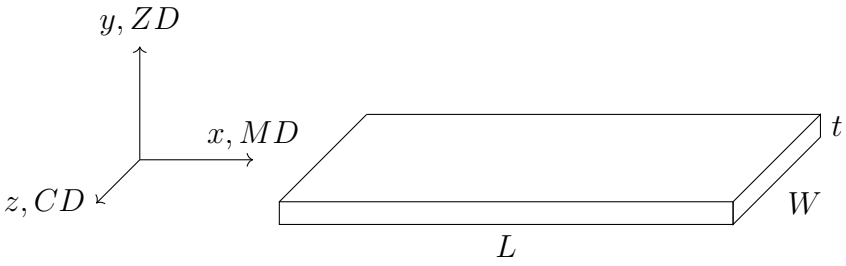

Figure 3: Geometry of the paperboard panel.

A male- and female die pair was modeled as two rigid bodies, with geometry given in Figure 4.

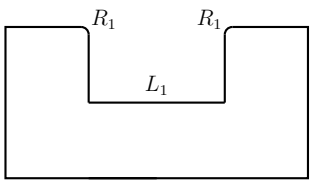

(a) Female die geometry

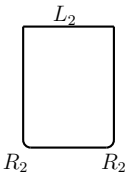

(b) Male die geometry

Figure 4: Female- and male die tool geometries with relevant geometric parameters marked out.

The values of the geometric entities in Figure 4 are given in Table 4:

	[mm]
L_1	1.25
L_2	0.6
R_1	0.05
R_2	0.05

Table 4: Geometric parameters presented in Figure 4.

Figure 5 illustrates the creasing operation steps.

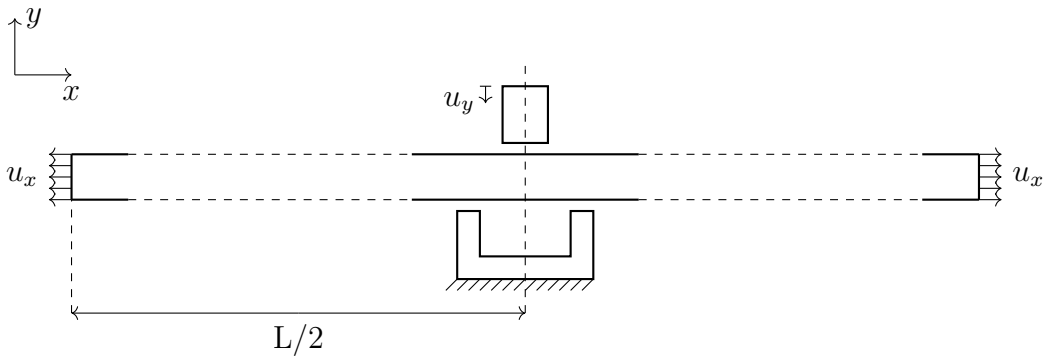

Figure 5: The paperboard is displaced u_x in both ends, in order to induce a specified in-plane force mimicking web tension. Creasing is then performed by displacing the male die by u_y towards the female die which is fixed in place.

It is noted that the creasing tools are moved into initial contact with the paperboard between the web tension- and creasing steps. After the required creasing depth of the male die is achieved, the male die displacement direction is reversed until it is no longer in contact with the paperboard. The creasing tools are then moved out of the way and the web tension is removed. Folding of the paperboard is later performed for a series of differing creasing depths. The creasing depths studied in the scope of this thesis are presented in the following table:

Crease depth index	1	2	3	4
u_y [mm]	0	0.45	0.6	0.75

Table 5: Different creasing depths simulated.

3.1.1 Creasing results

Although the creasing operation in itself is interesting, the scope of this thesis doesn't cover the creasing effect on paperboard in detail. The following figures presented in this subsection thus only illustrate the effects of creasing on the domain i.e how the paperboard domain is permanently deformed, without discussing the underlying mechanisms. Figure 6 shows the deformable paperboard domain before creasing:

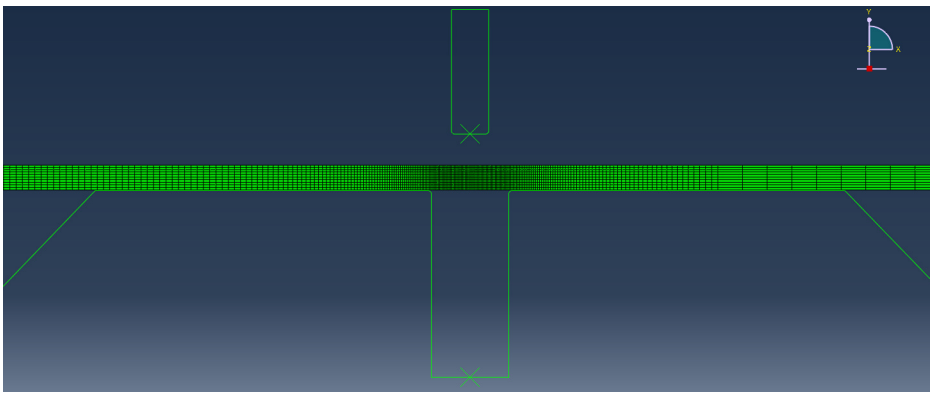

Figure 6: Creasing tools and paperboard section that is creased.

Figure 7a shows the Von Mises stress during the creasing, and Figure 7b the permanent deformation of the paperboard after creasing.

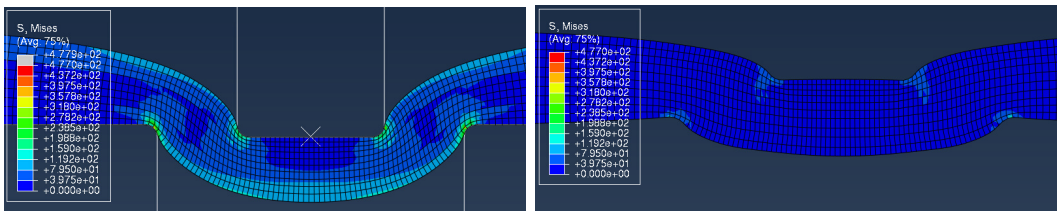

(a) Snapshot of creasing in mid-procedure (b) Creased paperboard segment

Figure 7: Creasing of paperboard.

Figure 8 show how the extent of permanent deformations increases as a result of deeper creasing.

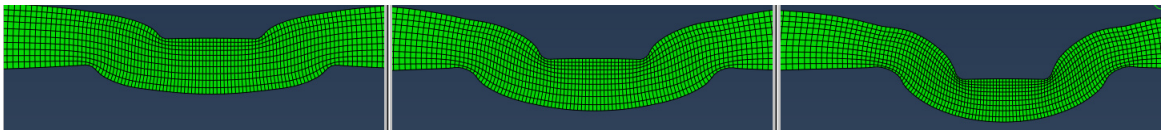

Figure 8: From left to right, creasing to depths 0.45 mm, 0.6 mm, 0.75 mm.

3.2 Folding

After creasing the paperboard, four rigid bodies are introduced. Two clamps are moved in to make contact with the paperboard, with the left clamp edges being positioned 1mm away from the crease center. Two loadcells denoted LCL and LCU are moved in to make contact with the paperboard, with the right edges of the load cells being positioned 10 mm away from the clamp left edges. The load cells are then fixed in space for the duration of the simulation. An illustration is provided in Figure 9:

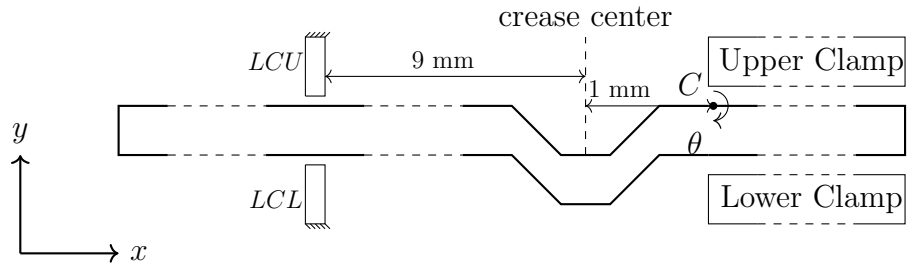

Figure 9: Simulation setup for folding of creased paperboard segment, partly corresponding to physical experiment setup.

The fold operation is actuated by rotating the rigid clamps around the reference point C which is located by the top clamp edge. While the clamps rotate θ (defined clockwise positive) around point C, the load cells measure reaction forces in both x- and y-components, though the y-component force is of main interest. The rotation of the clamps around C is also measured through the duration of the folding. Table 6 contains the folding sequences which were performed:

Simulation case	Creasing depth index	θ [°] - sequence
1	1,2,3,4	0, 90
2	3	0, 5, -5, 0
2	3	0, 45, -45, 0
3	3	0, 60, -60, 0
4	3	0, 75, -75, 0
5	3	0, 90, -90, 0
6	3	0, 105, -105, 0
7	3	0, -90, 90, 0
8	3	0, 90*

Table 6: The different load cases summarized, [*] denoting post folding compression of the crease described in a later subsection.

the simulation cases provide information about the impact of creasing depth on the initial fold response, the crease response to the folding direction being reversed, the impact of fold magnitude during reversal, and the crease model's behavior in a counter fold cycle. For details of simulation case 8 see Section 3.5.

3.3 Folding data

Figure 10 illustrates the deformation of the paperboard elements, Figure 10a shows the load cells on the left side constricting the vertical motion of the paperboard locally while allowing horizontal movement, while on the right side the two clamps rotate around the fixed point C. Figures 10b and 10c shows the development of the creased zone during the fold.

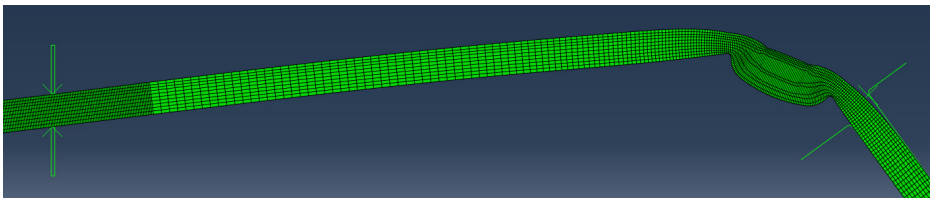

(a) Macroscopic view of loadcells, paperboard during fold and rotating clamps.

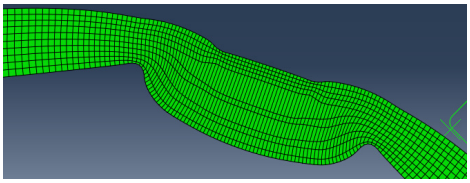

(b) 45 degree angle.

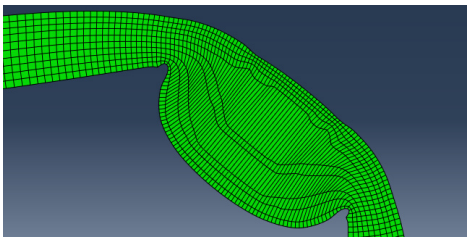

(c) 90 degree angle.

Figure 10: Snapshots from folding procedure.

3.3.1 Impact of creasing depth

Figure 11 contains the synthetic data corresponding to simulation case 1 in Table 6, corresponding to the creasing depths illustrated in Figure 8:

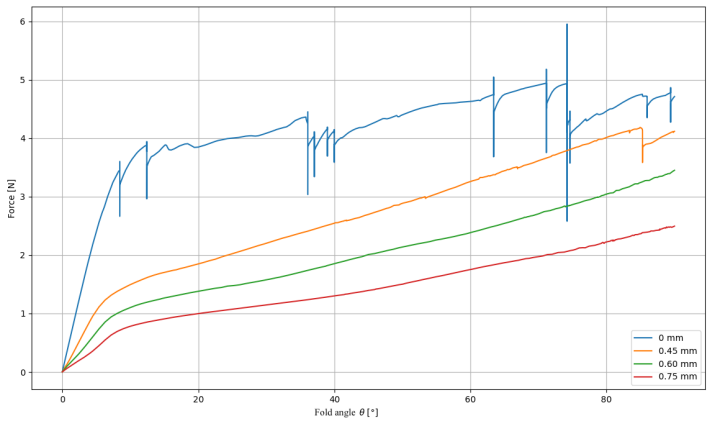

Figure 11: Vertical reaction force - fold angle curves for the different creasing depths, folding 0° to 90°.

3.3.2 Offloading

Figure 12 contains the synthetic data corresponding to simulation cases 2-6, where the creasing depth for each simulation was held constant at 0.6 mm.

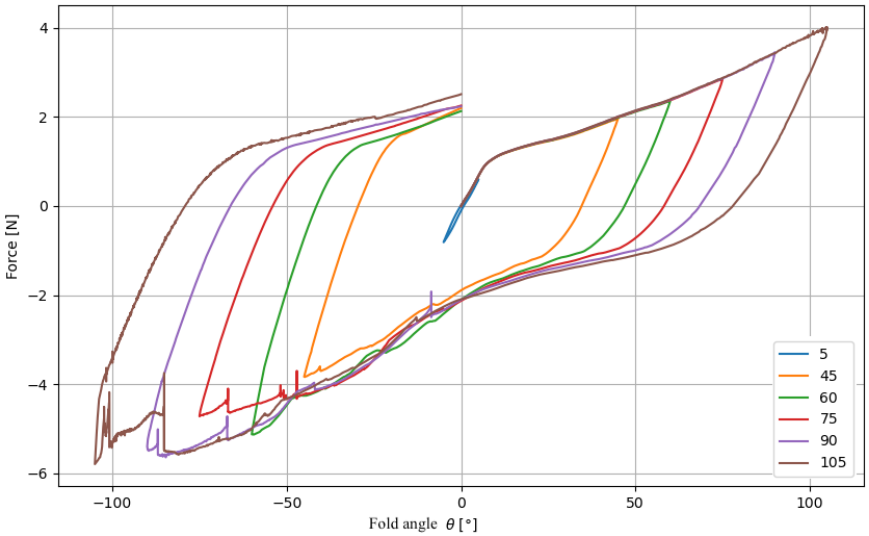

Figure 12: Fold cycles $[0, \theta, -\theta, 0]$, $\theta \in \{5, 45, 60, 75, 90, 105\}$, and corresponding reaction force from loadcells.

3.3.3 Counter folding

Figure 13 contains snapshots from simulation case 7, while Figure 14 contains obtained curves from case 7 along with case 5.

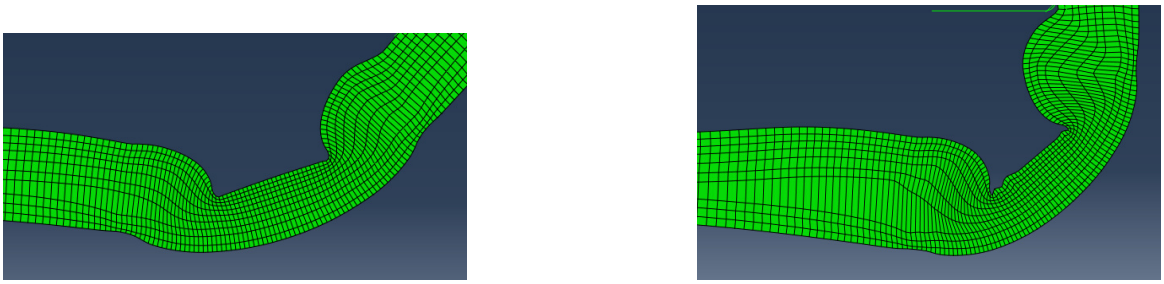

(a) -45 degree angle.

(b) -90 degree angle.

Figure 13: Snapshots from counter folding procedure.

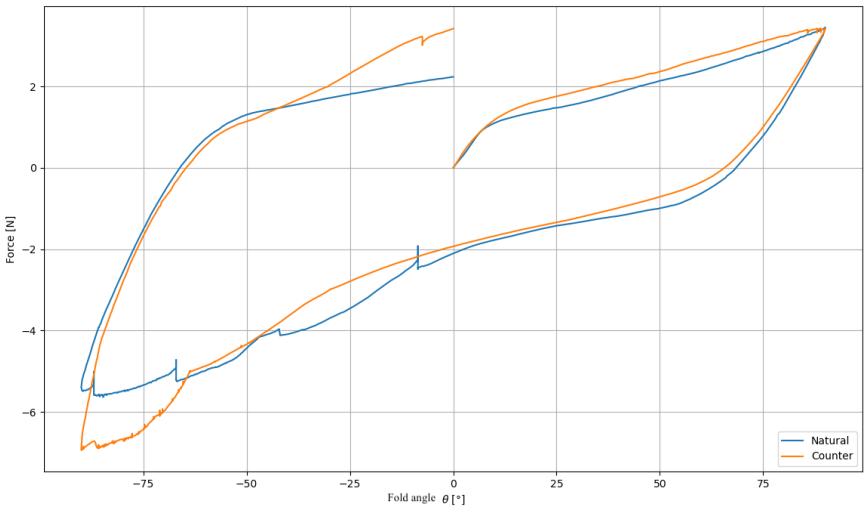

Figure 14: Comparisons of fold cycles $[0, 90, -90, 0]$ and $[0, -90, 90, 0]$, noting that the sign of the force- and rotation data has been flipped for the counter fold case for easier comparisons of the curves.

3.4 Folding Analysis

The force-fold angle curves relating to the different crease depths in Figure 11 can all be approximated as linear within the first 5 degrees of folding. The initial slope of the linear segments were estimated as $K = \frac{F_{\theta=5}}{5}$ $[N/°]$ and are plotted in Figure 15

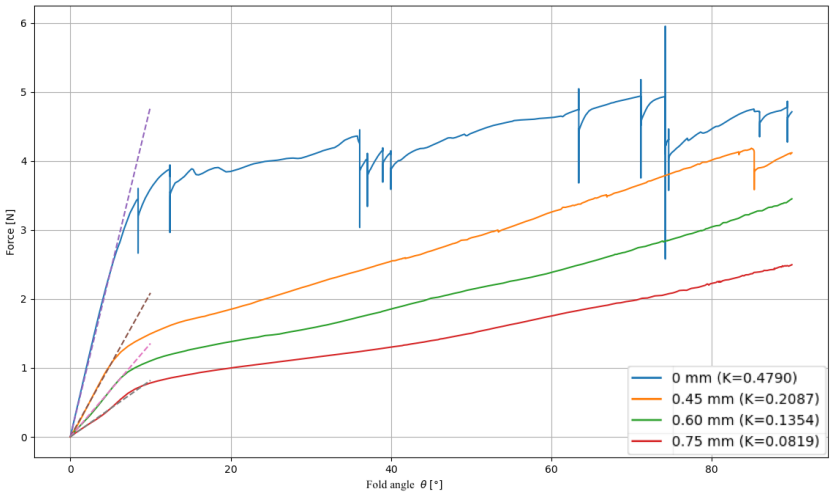

Figure 15: Slopes of approximated linear region $\theta \in [0, 5]$ at different creasing depths, computed K-value included in legend.

The linear slopes are also gathered in the following table:

crease depth	0 mm	0.45 mm	0.6 mm	0.75 mm
K $[N/°]$	0.4	0.2	0.1	0.08

Table 7: Linear slopes at 5 degree folding at differing crease depths.

As pointed out in Nagasawa et al. [5] there is a correlation between the creasing depth and the initial crease moment resistance, which is observed here as well, though no effort is made in this thesis to specify any relation between the two quantities. Regarding the crease material's constitutive behavior the first 5 degrees of folding could be regarded as within a linear elastic regime, consider Figure 16 containing the 5 degree curve from Figure 12:

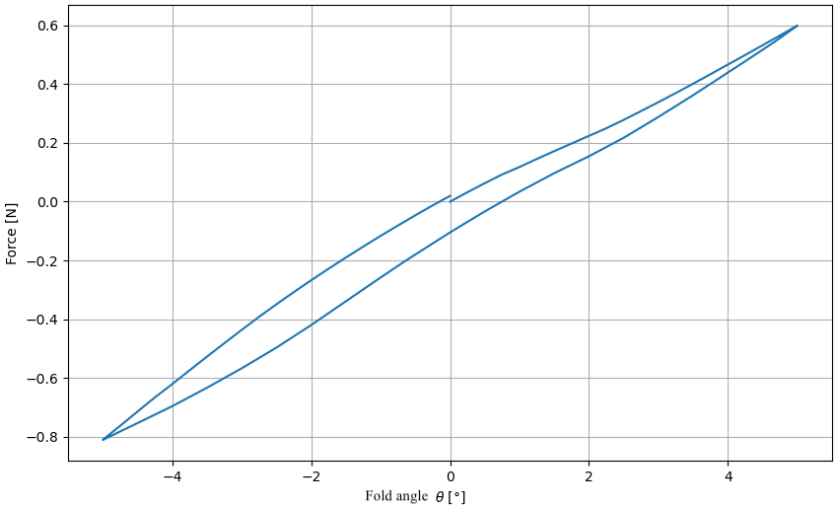

Figure 16: Fold cycle $[0, 5, -5, 0]$ and corresponding reaction force from loadcells.

After folding up to 5 degrees and folding back to 0 degrees a residual force of approximately 0.1 N acts on the load cells, which in relation to the approximate residual force of 2 N acting on the load cells from the other load cycles illustrated in Figure 12 is relatively small. After a full 5 degree cycle the residual force is approximately 0.01 N, indicating that the creased paperboard has underwent very minor permanent deformations.

Studying the fold cycle curve $[0, 90, -90, 0]$ in Figure 17 some macroscopic behaviors can be observed. After 5 degrees of folding the curve tangent slope steadily decreases, indicating a change in behavior of the crease due to yielding and development of plastic strains.

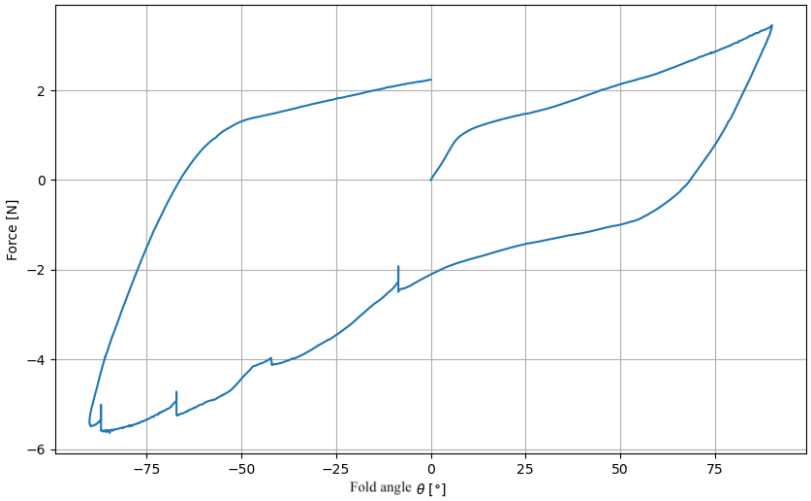

Figure 17: Fold cycle $[0, 90, -90, 0]$ and corresponding reaction force from loadcells.

From 10 degrees of folding up to 90 degrees the force response steadily increases in a seemingly linear if not lightly quadratic manner, a behavior not observed in [5], though as previously mentioned typical of the Borgqvist model which overestimates the stiffness of the crease in folding. The curve in offloading after 90 degrees of folding appears to be linear in an angle-interval larger than the initial 0 to 5 degree linear interval, indicating that the size of the elastic regime has increased. The transition of linear- to nonlinear behavior in the offloading is also more gradual than in the initial 0 to 90 folding sequence. Angles 20 to -20 in the offloading by hardening of the board response, this could correlate with the fold going from a natural one to a counter-type fold. Alternatively, the placement of the rotation point C could have an influence. Further investigations involving varying the location of C across the paperboard thickness could be conducted. Particularly for complex folding sequences, centering its location within the paperboard may be optimal, ensuring symmetry for the fold of the clamps. The final part of the cycle going from -90 to 0 degrees of folding also points toward an increase in the size of the elastic regime, but also initial stiffness that is higher than previously observed.

Figure 12 indicates that some form of saturation of the bending resistance occurs when folding between angles θ to $-\theta$ for $\theta \in 45, 60, 75, 90, 105$, clearly seen in the point (0,-2). The same phenomena is observed again when folding between angles $-\theta$ to 0. Figure 14 indicates that the crease seems to respond in a similar manner in regards to folding stiffness regardless of the folding direction, this despite the apparent geometric asymmetry. Due to the lack of experimental data this model prediction can't be verified, but is useful in the context of this work since the result indicates that no asymmetry has to be taken into consideration regarding natural- or counter folding which was schematically illustrated in Figure 14. The sudden increase in force between angles -62.5 to -90 degrees and -40 to 0 degrees in the counter folding curve is due to direct contact between the folding tools and the crease.

Finally, it was observed in all simulated cases that the plastic strains were concentrated to a small area containing the crease and neighboring elements, implying that the rest of the paperboard can be approximated as fully elastic in the context of the beam approximated folding simulation.

3.5 Compression

After folding about the crease, the paperboard is moved in place for a compression test of the crease. A rigid body plate is introduced and moved into position above or below the crease depending on the final fold angle, while the paperboard is clamped on the side running parallel with the plate. The plate acts as a wall, fixed in space and measures the reaction forces. This particular test is inspired by Beldie, cf. [18]. Figure 18a illustrates the setup:

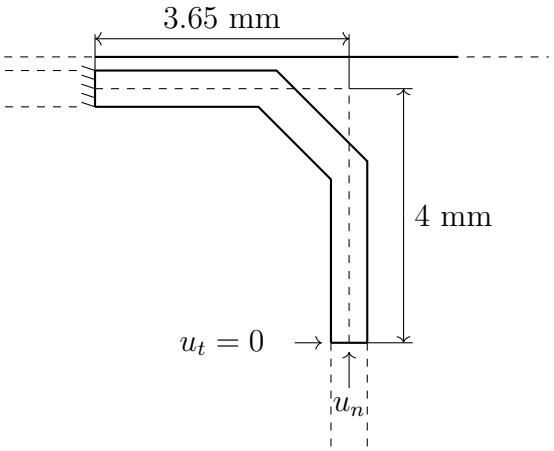

(a) Rig for compression test of the crease in virtual environment.

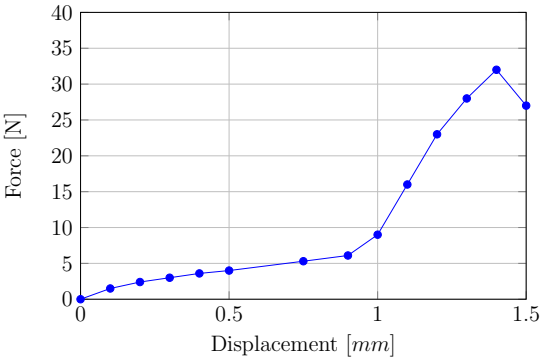

(b) Data interpolated from crease compression test in [18].

Figure 18: Setup for crease compression test in this thesis and the experimental data that is to be compared.

The nodal displacement of the paperboard on the side not parallel with the clamp is controlled such that u_n normal to the local ZD-direction is increased, while u_t tangent to the the local ZD-direction is fixed. In the scope of this thesis only a 90 degree fold followed by compression is considered, resulting in $u_n = u_y$, $u_t = u_x$. Figure 18b contains an interpolated curve from the experimental data in [18]. While there exists differences in the test rig configurations between the referenced study and this work, the dataset serves as a macroscopic comparison against the results of this work.

3.5.1 Compression data and analysis

Figures 19a to 19e display compression of the crease at various stages of displacement, while Figure 20 shows the resulting force-displacement curve.

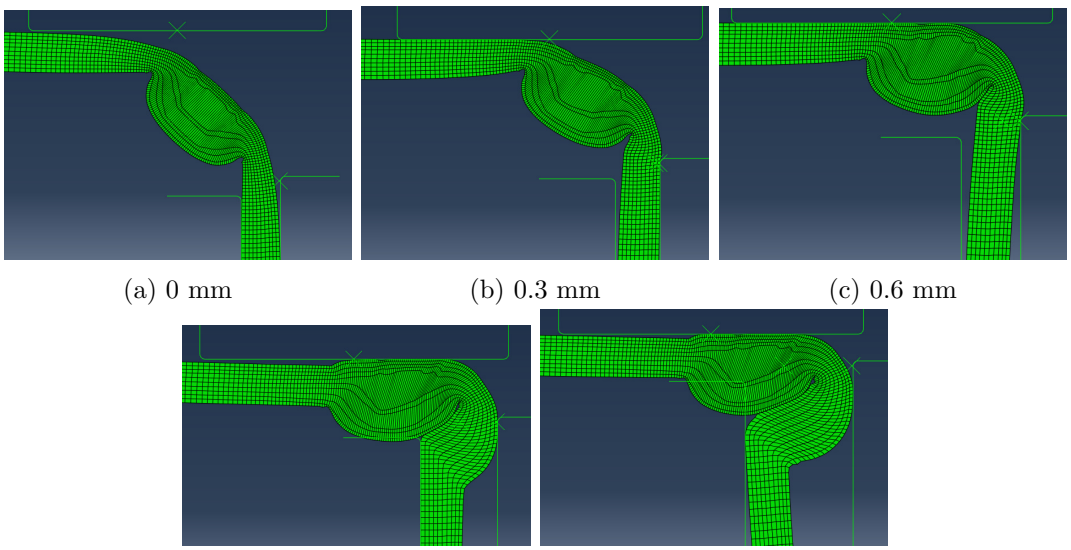

(a) 0 mm (b) 0.3 mm (c) 0.6 mm

(d) 0.9 mm (e) 1.2 mm

Figure 19: Compression of crease at different displacements

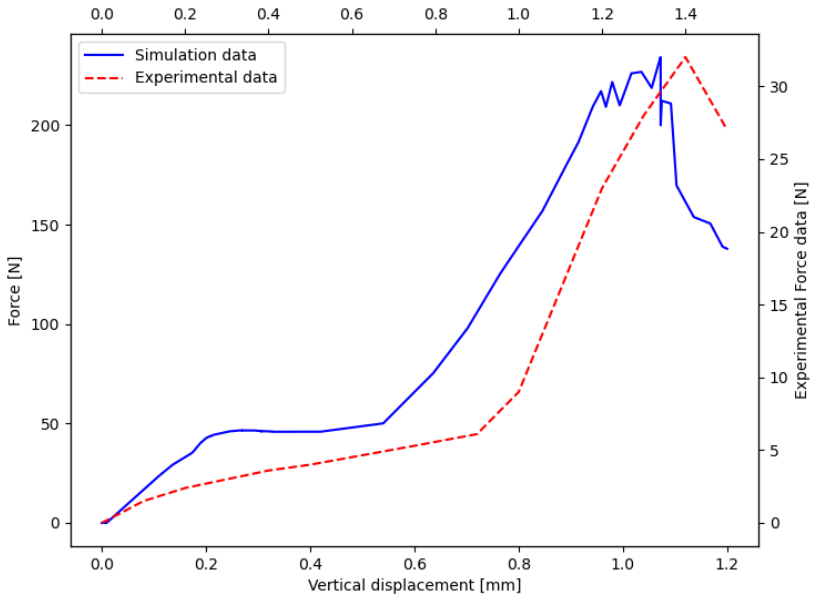

Figure 20: Experimental data[18] and synthetic results.

Figure 20 compares the synthetic compression data with the experimental data, on separate x-y axes but in the same graph. The initial 0.2 mm of displacement of the simulation data is characterized by the increase in contact area between the fixed plate and noncreased paperboard. Disregarding that part of the compression, both the experimental and synthetic curves show an initially weak response. Figures 19b and 19c indicate that the crease is compliant with the motion until it flattens out against the plate, marking a sudden increase in stiffness. Similar observations were made by Beldie [18] indicating that the Borgqvist model has predictive capabilities in loading situations it hasn't been directly calibrated against previously.

4 Beam Element Approximation

A simplified approximation of the crease folding was made, replacing the previously approximated continuum domain with beam elements. All of the modeling tools that are utilized in the following subsections already exist in Abaqus, which reduces the complexity of implementation significantly, especially with regards to both the theoretical formulation and code implementation of geometrically- and materially nonlinear user defined elements (UEL) and/or user defined materials (UMAT).

The paperboard domain is modeled to be fully comprised of beam elements, with a single beam that is used to model the crease. In this modeling approach, the creasing operation is omitted, instead the crease beam is calibrated beforehand using experimental or synthetic folding data. By performing a parametric study of geometric and material properties of the crease beam some basic relations might be identified that can be utilized for calibration purposes. Consider Figure 21, similar to Figure 9 but using the two dimensional coordinate plane x-z for more consistent notation:

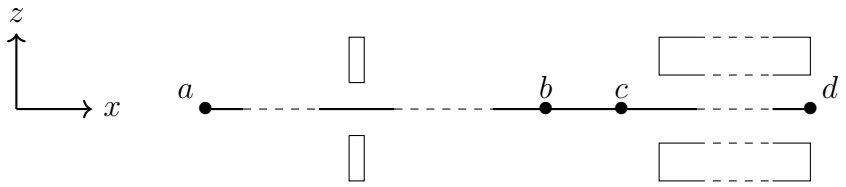

Figure 21: Simulation setup for folding of creased paperboard segment using a beam approximation.

Segments ab and cd in Figure 21 represent noncreased paperboard which is modeled using a fully elastic orthotropic constitutive law, while segment bc is the single beam element which constitutive law is to be modified in order to represent the crease. The distance bc in Figure 21 is the same as the length of the female die tool given in Table 4, while the other geometric distances are the same as those specified in Figure 9. The cross sections for the beam segments were modeled as rectangular and are shown in Figures 22a and 22b:

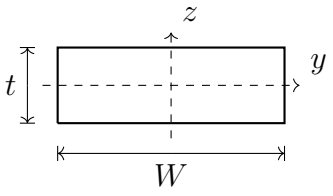

(a) Initial cross section of noncreased paperboard beam segments ab and cd, assigned the same thickness and width as the paperboard in the continuum approximation.

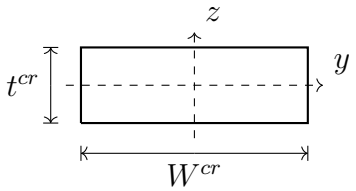

(b) Initial cross section of creased paperboard beam segment bc, with thickness t^{cr} and width W^{cr}, superscript [^{cr}] denoting creased

Figure 22: Geometry of the beam approximated paperboard model.

Analysis of Figure 22 results in the following expressions for the beam cross sectional area A and area moment of inertia I_{yy}:

$$A = t \cdot W \qquad (1)$$

$$I_{yy} = \frac{1}{12} t^3 \cdot W$$

$$A^{cr} = t^{cr} \cdot W^{cr} \qquad (2)$$

$$I_{yy}^{cr} = \frac{1}{12} (t^{cr})^3 \cdot W^{cr}$$

The two dimensional beams in Figure 21 subjected to a bending moment M_b or axial force N relate to the stress state of a cross section via:

$$M_b = \int_A \sigma_{xx}(z) \cdot z \; dA \qquad (3)$$

$$N = \int_A \sigma_{xx}(z) \; dA \qquad (4)$$

and illustrated in Figure 23:

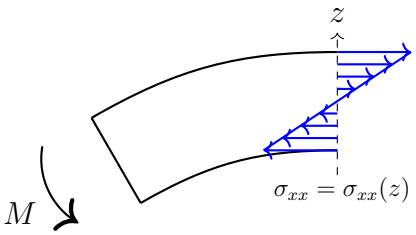

(a) Stress distribution in cross-section of beam in pure bending.

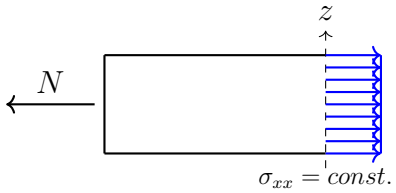

(b) Stress distribution in cross-section of beam subjected to monotonic axial load.

Figure 23: Stress state of a beam cross section dependent on the mode of loading.

where $\sigma_{xx}(z)$ is the cross sectional normal stress, which in bending varies throughout the cross section in z-direction, $z \in [\frac{-t}{2}, \frac{t}{2}]$. The integration of the analytical expressions (3) and (4) is performed numerically by Abaqus during the finite element analysis by utilizing five Simpson type integration points throughout the cross sectional height [22].

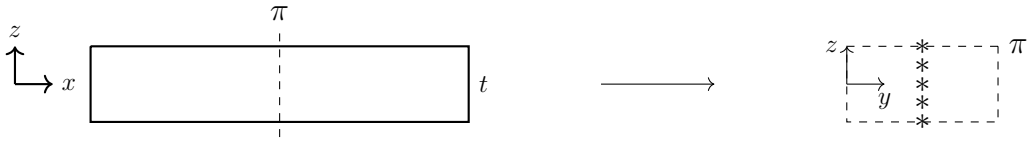

Figure 24: Left: Analytical beam axially oriented in x-direction, right: allocation of the five integration points (*) through the cross section height

4.1 Linear Elastic Material Model

The noncreased beam segments were assigned an orthotropic linear elastic material model, with the compliance matrix $\mathbf{C}$ defined by $\boldsymbol{\epsilon} = \mathbf{C}\boldsymbol{\sigma}$, in which $\boldsymbol{\epsilon}$ denotes the strain tensor and $\boldsymbol{\sigma}$ the stress tensor, all in Voigt-notation.

$$\mathbf{C} = \begin{bmatrix} \frac{1}{E_x} & -\frac{\nu_{yx}}{E_y} & -\frac{\nu_{zx}}{E_z} & 0 & 0 & 0 \\ -\frac{\nu_{xy}}{E_x} & \frac{1}{E_y} & -\frac{\nu_{zy}}{E_z} & 0 & 0 & 0 \\ -\frac{\nu_{xz}}{E_x} & -\frac{\nu_{yz}}{E_y} & \frac{1}{E_z} & 0 & 0 & 0 \\ 0 & 0 & 0 & \frac{1}{G_{xy}} & 0 & 0 \\ 0 & 0 & 0 & 0 & \frac{1}{G_{xz}} & 0 \\ 0 & 0 & 0 & 0 & 0 & \frac{1}{G_{yz}} \end{bmatrix} \tag{5}$$

it is also noted that the component ordering of the tensor terms in Voigt notation is that of [xx yy zz xy xz yz] cf. [23] where $x = 1$, $y = 2$, $z = 3$. Due to symmetry $\mathbf{C}_{12} = \mathbf{C}_{21}$, $\mathbf{C}_{13} = \mathbf{C}_{31}$ and $\mathbf{C}_{23} = \mathbf{C}_{32}$, the noncreased segment's linear elastic behavior is thus fully defined by the parameters in the following table:

	[MPa]
E_x	6785
E_y	3150
E_z	31.44

	[MPa]
G_{xy}	1788
G_{xz}	230.9
G_{yz}	157.4

	[-]
ν_{xy}	0.43
ν_{xz}	0
ν_{yz}	0

Table 8: Values of Young's modulus E_i, shear modulus G_{ij} and Poisson's ratios ν_{ij} for the orthotropic material, $i \in x, y, z$

The tabular data corresponds to the same material used in the synthetic data acquisition. The creased paperboard segment material model was approximated as similar to the uncreased beams, but even simpler, by ignoring the Poisson effect ($\nu_{xy} = 0$). The resulting $\mathbf{D}^{cr}$-matrix defined by:

$$\boldsymbol{\sigma}^{cr} = \mathbf{D}^{cr}\boldsymbol{\epsilon}^{cr} \tag{6}$$

is formulated as:

$$\mathbf{D}^{cr} = \begin{bmatrix} E_x^{cr} & 0 & 0 & 0 & 0 & 0 \\ 0 & E_y^{cr} & 0 & 0 & 0 & 0 \\ 0 & 0 & E_z^{cr} & 0 & 0 & 0 \\ 0 & 0 & 0 & G_{xy}^{cr} & 0 & 0 \\ 0 & 0 & 0 & 0 & G_{xz}^{cr} & 0 \\ 0 & 0 & 0 & 0 & 0 & G_{yz}^{cr} \end{bmatrix} \tag{7}$$

where it is assumed that all parameters except E_x^{cr} equal the corresponding noncreased parameter.

4.2 Linear Curve Region

From (6) and (7) it is evident that $\sigma_{xx}^{cr} \propto E_x^{cr}$, which along with (2), (3) and (4) results in the following relations also being proportional:

$$M_b^{cr} \propto E_x^{cr} \cdot I_{yy}^{cr} \tag{8}$$
$$N^{cr} \propto E_x^{cr} \cdot A^{cr} \tag{9}$$

i.e the bending moment a beam's cross section is proportional to its area moment of inertia and the local direction elastic modulus, while the normal force N of a cross section is proportional to the cross sectional area and the local direction elastic modulus. Postulating that creased paperboard's loss of stiffness in monotonic axial loading is mainly a result of material property damage, i.e $E_x^{cr} < E_x$ and $A^{cr} \approx A$, and that the weakened bending stiffness is a result of decreased area moment of inertia, $I_{yy}^{cr} < I_{yy}$, enables the following relations to be defined:

$$A^{cr} = A \tag{10}$$
$$I_{yy}^{cr} = I_{yy}^{cr}(\alpha) = I_{yy} \cdot (1 - \alpha) \tag{11}$$
$$E_x^{cr} = E_x^{cr}(\beta) = E_x \cdot (1 - \beta) \tag{12}$$

where α and β are scaling parameters, which are used to replicate the linear slope at 0.6 mm creasing presented in Table 7. $(\alpha, \beta) = (0, 0)$ corresponds to the same initial slope as that of the noncreased paperboard folding result in Table 7, while $(\alpha, \beta) = (1, 1)$ corresponds to a void-material in the creased zone (no stiffness), thus values of $\alpha, \beta \in [0, 1)$ are studied resulting in datapoints characterizing the relation $K = K(\alpha, \beta)$. In practice the area moment of inertia is changed by altering t^{cr} and W^{cr}, by using (1), (2), (10) and (11):

$$t^{cr} = \sqrt{1 - \alpha} \cdot t \tag{13}$$
$$W^{cr} = \frac{1}{\sqrt{1 - \alpha}} \cdot W \tag{14}$$

In Abaqus, the manipulation of the area moment of inertia while preserving the predefined cross-sectional area is simple by using beam elements. Section properties can be changed in the graphical interface. Similar possibilities don't exist for shell elements, which necessitates the use of a user-defined element subroutine (UEL). Since the shell element width and length is defined in Abaqus by its' constitutive nodes, only the thickness is available for manipulation in the graphical interface.

4.3 Plastic Onset and Hardening Characteristics

In Figure 15 the initial slope K of the linear elastic area deviates due to yielding, subsequently weakening the bending stiffness further. By approximating paperboard

folding as pure bending of a beam, any shear forces can thus be neglected, resulting in σ_{xx} being the only nonzero stress component. The subsequent plasticity modeling reduces to a one dimensional problem. Von Mises' yield surface F is utilized in order to elastic regime, resulting in:

$$F = |\sigma_{xx}| - \sigma_{y0} \tag{15}$$

which is evaluated in each integration point of the beam element. σ_{y0} defines the initial yield stress of the beam material, determining the size of the initial elastic regime as shown in Figure 25:

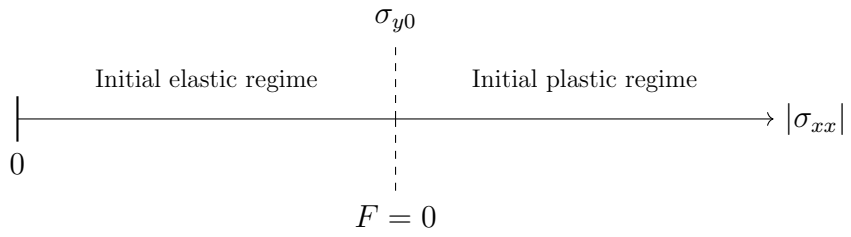

Figure 25: Yield surface reduced to a single axis representation

The initial elastic regime is limited to $F < 0$ and characterizes a fully elastic response for an individual integration point. Plastic yielding is initialized at $F = 0$, the response of an individual integration point response becomes elasto-plastic. The initial yield stress was related to Young's modulus E_x via the following relation:

$$\sigma_{y0} = \gamma \cdot E_x \tag{16}$$

which introduces γ as a third parameter to study. The development of plastic strains moves the initial yield surface boundary, which necessitates a description of the current yield surface f, initially modeled using an isotropic hardening law:

$$f = |\sigma_{xx}| - \sigma_y \tag{17}$$

$$\sigma_y(\varepsilon^p_{xx}) = \sigma_{y0} + \Xi(\varepsilon^p_{xx}) \tag{18}$$

where $\sigma_y(\varepsilon^p_{xx})$ is the yield stress for a given plastic strain ε^p_{xx}. Ξ is the function that characterizes the yield stress - plastic strain relationship. Figure 26a illustrates the yield stress evolution, while Figure 26b illustrates the evolution of the yield surface subject to an isotropic hardening law:

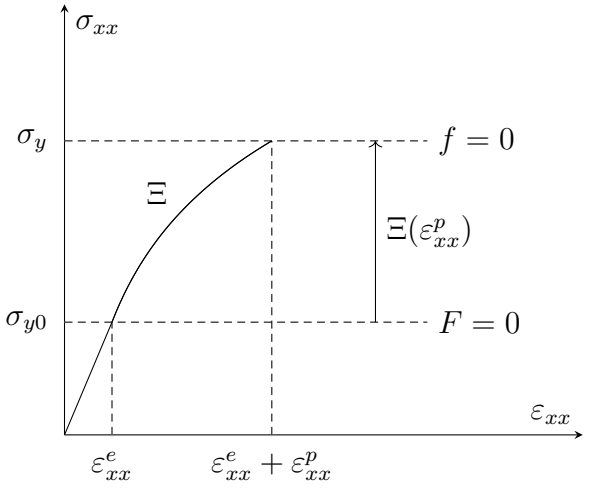

(a) Yield stress evolution for tensile loading, $\Xi(\varepsilon^p_{xx})$ defines the expansion of the elastic regime as a result of plastic loading

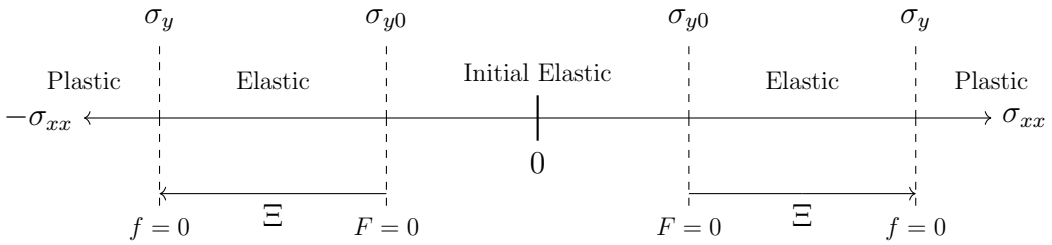

(b) Isotropic Hardening: uniform expansion of elastic regime which center remains fixed, in this case around 0

Figure 26: Hardening rate and hardening law

In the linear elastic regime the material stiffness is defined Young's modulus, in the plastic loading regime the material stiffness is also influenced by the plastic hardening modulus $d\Xi/d\varepsilon^p_{xx}$ which is dependent on the current plastic strain ε^p_{xx}. The following functions characterizing the yield stress evolution were considered in separate parameter studies:

$$\Xi_{lin}(\zeta, \varepsilon^p_{xx}) = \sigma_{y0} \cdot \zeta \varepsilon^p_{xx} \tag{19}$$

$$\Xi_{quad}(\zeta, \eta, \varepsilon^p_{xx}) = \sigma_{y0} \cdot (\zeta \varepsilon^p_{xx} + \eta(\varepsilon^p_{xx})^2) \tag{20}$$

Ξ_{lin} denotes a linear relation and Ξ_{quad} a quadratic relation. ζ and η are introduced parameters to study the behavior of the different functions. By supplying data points for $\sigma_y = \sigma_y(\varepsilon^p_{xx})$, Abaqus utilizes the data in conjunction with an associated flow rule in order to characterize the plastic evolution, see Table 9. [22]

Yield Stress	Plastic Strain
σ_{y0}	0
σ_y^1	$\varepsilon_{xx}^{p,1}$
$\vdots$	$\vdots$
σ_y^i	$\varepsilon_{xx}^{p,i}$

Table 9: First row of tabular data determines initial yielding, following i rows of data characterizes the hardening behavior, $\varepsilon_{xx}^{p,i-1} < \varepsilon_{xx}^{p,i}$

4.4 Isotropic and Kinematic Partitioning

Two different hardening behaviors are available in order to characterize the yield surface behavior, isotropic- and kinematic hardening. Isotropic hardening was described in the previous section, while kinematic hardening is modeled via the following relation:

$$f = |\sigma_{xx} - \Xi| - \sigma_{y0} \tag{21}$$

where Ξ now instead represents a back-stress, which uniformly moves the yield surface in the direction of loading, illustrated in Figure 27:

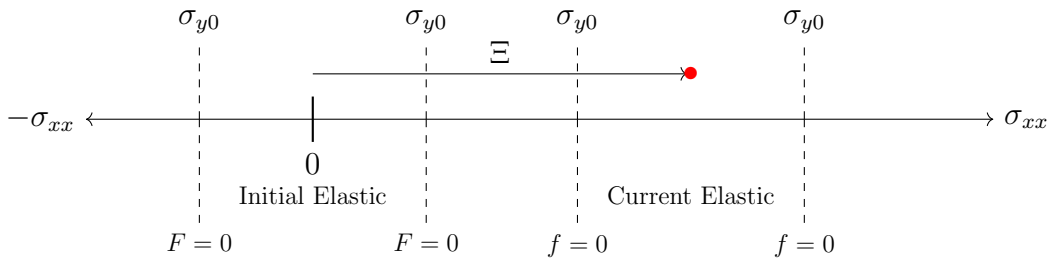

Figure 27: Kinematic Hardening: uniform motion of elastic regime in the direction of yielding, in this case tensile loading, where • represents the back-stress variable moving the surface

A combination of the hardening laws, known as combined hardening, enables the yield surface to both move in the direction of loading and expand simultaneously. This can be modeled as:

$$f = |\sigma_{xx} - \Xi_{kin}| - (\sigma_{y0} + \Xi_{iso}) \tag{22}$$

where subscripts $[_{kin}]$ and $[_{iso}]$ denote the yield surface's kinematic and isotropic behaviors respectively. This modeling approach isn't directly available in Abaqus unless it is implimented via a subroutine. Instead two curves are characterized, the first curve providing the position of the yield stress surface boundary as a function of plastic strain, the second curve providing the size of the yield surface as a function of the plastic strain, in Figure 28 the curves are denoted Ξ and Ξ_{iso} respectively:

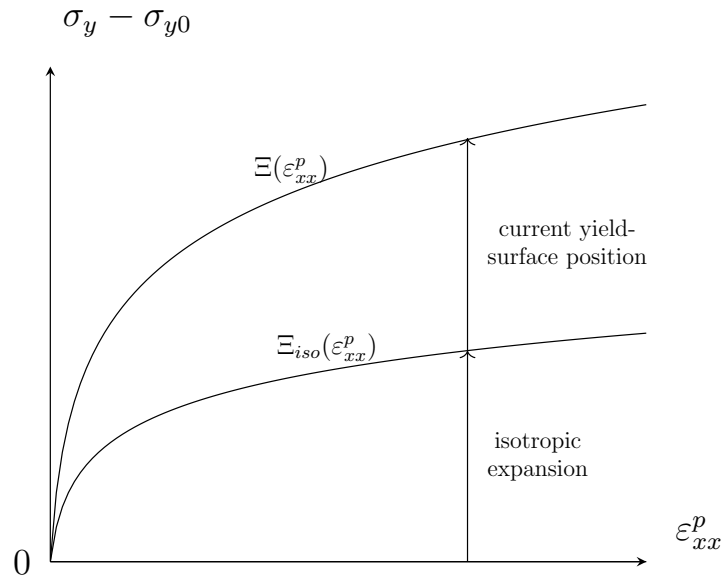

Figure 28: Method of modeling combined hardening in Abaqus

The isotropic expansion Ξ_{iso}, was modeled as:

$$\Xi_{iso}(\varepsilon^p_{xx}) = \mu \cdot \Xi(\varepsilon^p_{xx}) \tag{23}$$

where $\mu \in [0, 1]$, $\mu = 0$ corresponding to pure kinematic hardening while $\mu = 1$ corresponds to pure isotropic hardening. This concludes the definition of parameters subject to the study, to summarize:

α, β: Linear bending- and monotonic axial load stiffness parameters

γ: Plastic onset parameters

ζ, η: Plastic hardening parameters

μ: Hardening mode parameter

5 Results and Discussion

5.1 Initial Linear Regime

The force-fold angle curve of noncreased paperboard material in the continuum- and beam approximation case is shown in Figure 29. The computed K-values included in the figure show that the beam approximation is about 21% stiffer in the folding response, though since folding of noncreased paperboard is not of interest this difference isn't studied in more detail, rather it only indicates that the beam approximation yields results of the same magnitude as the continuum approximation.

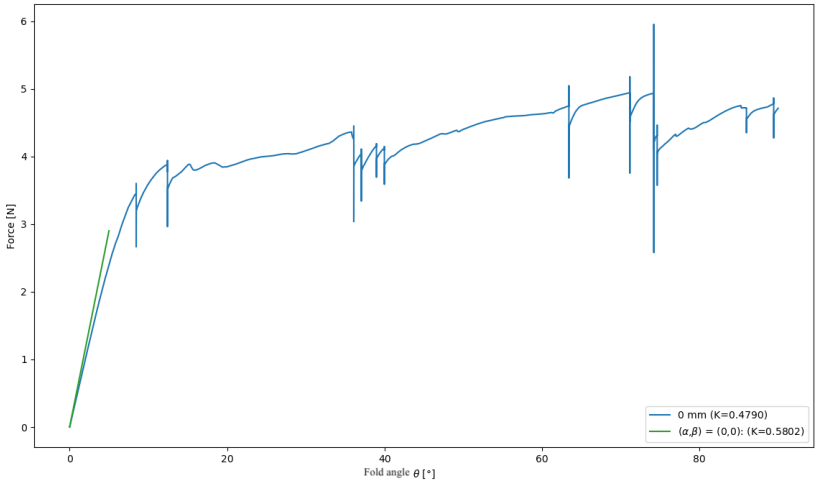

Figure 29: Bending stiffness curves of continuum- and beam approximation folding 0 to 90 degrees and 0 to 5 degrees respectively, for the crease beam $(\alpha, \beta) = (0, 0)$.

Figure 30 contains a selection of folding results, specifically force-fold angle curves for pairs (α, β) where $\alpha = \beta$, along with synthetic folding data for 0 mm and 0.6 mm of creasing for reference.

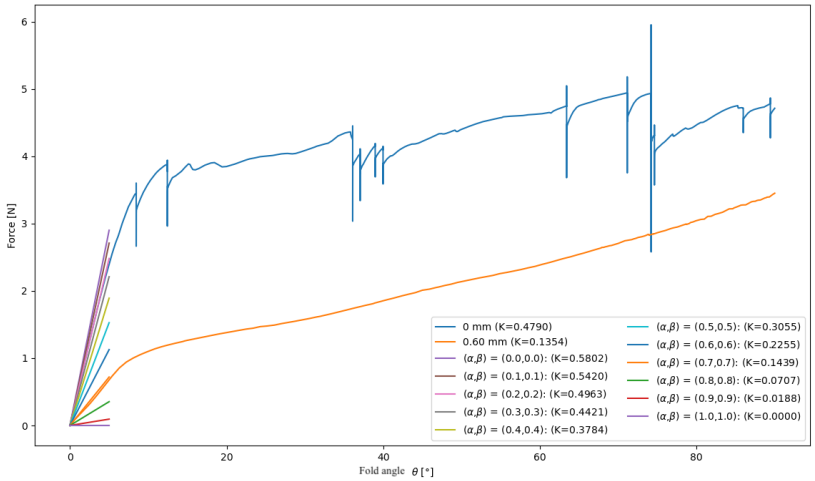

Figure 30: Bending stiffness curves from synthetic data, along with $\alpha = \beta$ curves (zero stiffness curves $\alpha = \beta = 0$ assumed)

The variation of K-values in Figure 30 covers the full spectrum of K-values found in the synthetic data in Table 7, vizualized by plotting K on a third axis as $K = K(\alpha, \beta)$, shown in Figure 31. Increased values of α and/or β results in a reduction of initial stiffness.

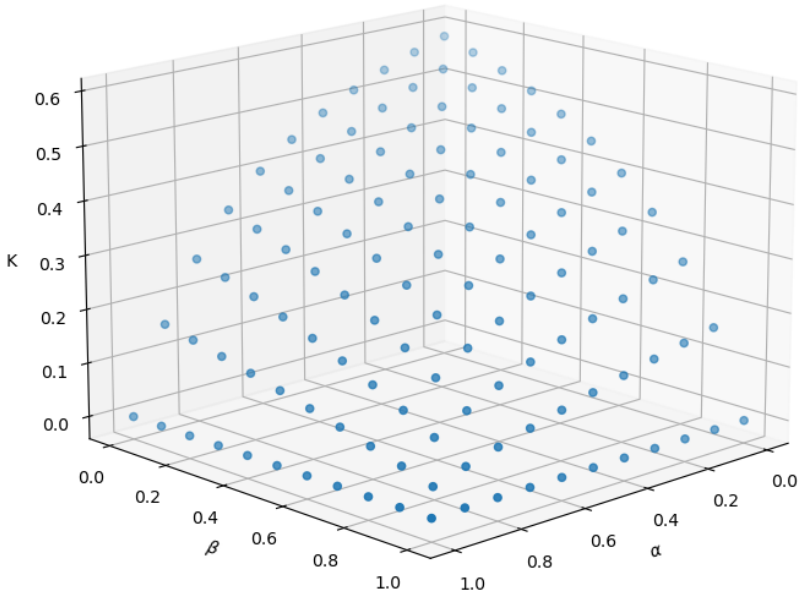

Figure 31: Initial bending stiffness $K = K(\alpha, \beta)$

Piecewise linear isoline-curves of the points in Figure 31 are shown for fixed values of β in Figure 32:

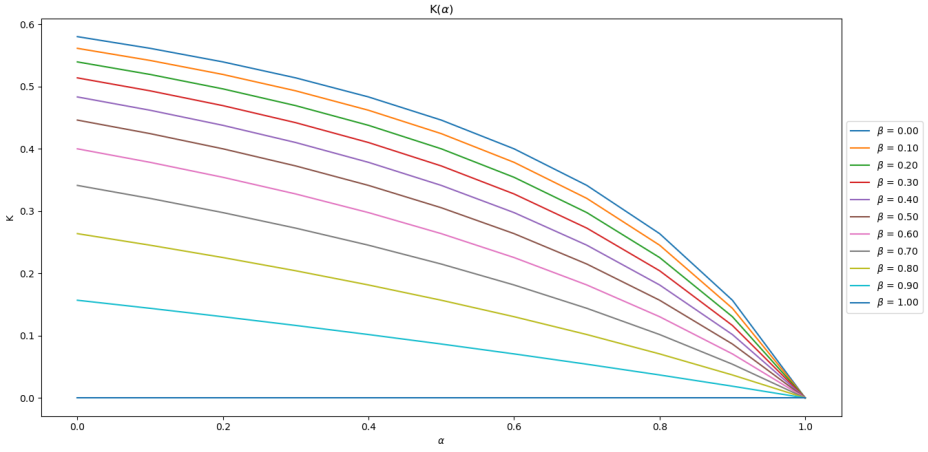

Figure 32: Isolines of $K(\alpha)$ for fixed β values. $K(\beta)$ for fixed α values produces an identical graph

Figures 31 and 32 show that for a given K-value there exists in a plane multiple combinations of α and β corresponding to the same initial bending stiffness, which offers flexibility in the modeling approach when calibrating the beam, for instance calibrating the beam to both capture a creased paperboard's response in both monotonic axial

loading while simultaneously calibrating the bending stiffness, representing equations (4) and (3) respectively. The points in Figure 31 could be modeled as a continuous surface, the symmetry of the point distribution is likely due to both E_x and I_{yy} being linearly proportional to M_b. A pair (α, β) was interpolated to $(0.914, 0)$ in order to match K from the synthetic 0.6 mm crease fold-curve.

5.2 Yielding and Hardening Characteristic

Figure 33 contains force-fold angle curves using the previously chosen (α,β) pair, the different curves signifying different values for γ. The yield stress - plastic strain relations for all curves were modeled as ideal plastic by using Ξ_{lin} where $\zeta = 0$, and as previously the reference synthetic data curve folding after 0.6 mm creasing is included:

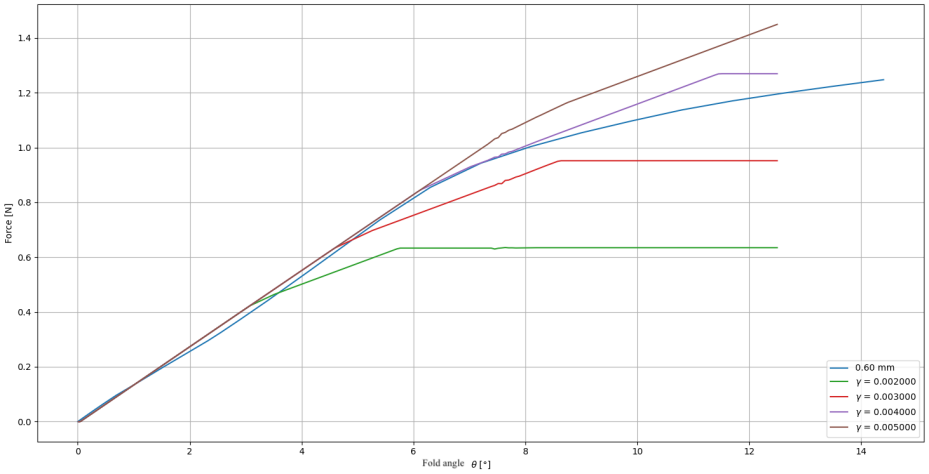

Figure 33: Plastic Yielding initiation for different values of γ, ideal-plastic hardening

All beam curves adhere to the same initial bending stiffness, around 3 degrees of folding the curve corresponding to γ_{min} diverges in a weakening manner. The same behavior is observed for increasing γ-values at increased degrees of folding, reasonable since γ scales the initial yield stress. It is also possible to observe the occurrence of two yield points for each curve (except the synthetic curve and γ_{max}), this is due to the order in which the integration points throughout the beam element enter yielding, the outer integration points are subject to more straining during bending than the inner integration points and thus represent the first yield of the curves. After the outer integration points yield the force-rotation curve is characterized by a simultaneous plastic and elastic behavior, until the inner integration points are strained to such a degree that the second second yield of the curves (for γ_{min} around 5.5 degrees).

Figure 34 contains an excerpt of the parametric study results for the linear stress - plastic strain hardening characterization, with Figure 34c showing the most promising fit.

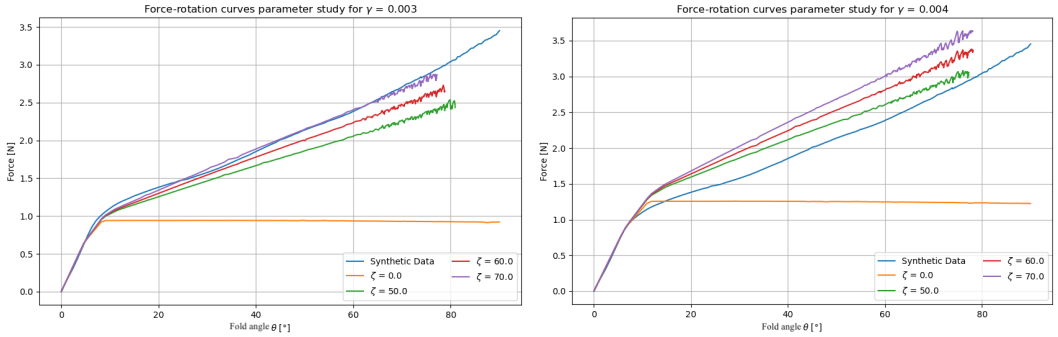

(a) (b)

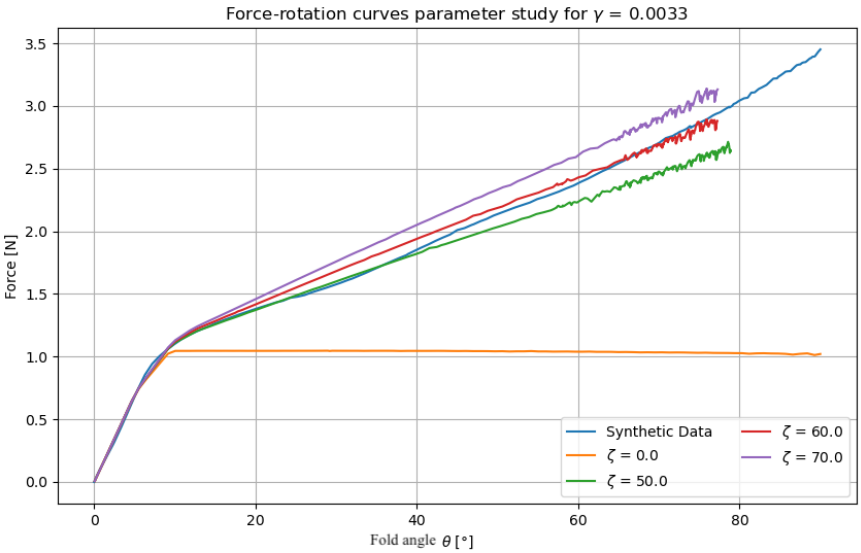

(c)

Figure 34: Linear yield stress - plastic strain curves for different γ and ζ

Figure 34 also show that choice of γ to proceed with isn't obvious from the result in Figure 33, since ideal plasticity was assumed its effect on the bending stiffness is present in the folding regime between the two diverging points. Instead including γ as a parameter when characterizing the plastic hardening was necessary. It's noted that the fluctuations occurring towards the end of the curve related to the beam approximation is likely caused by contact between the paperboard and the load cells. A harsher contact formulation resulted in numerical instabilities, while relaxing the contact penalty parameters instead induce small oscillations at higher loads. Having performed a parametric study using the quadratic plasticity function Ξ_{quad}, along with manually refining the parameters the following curve was obtained:

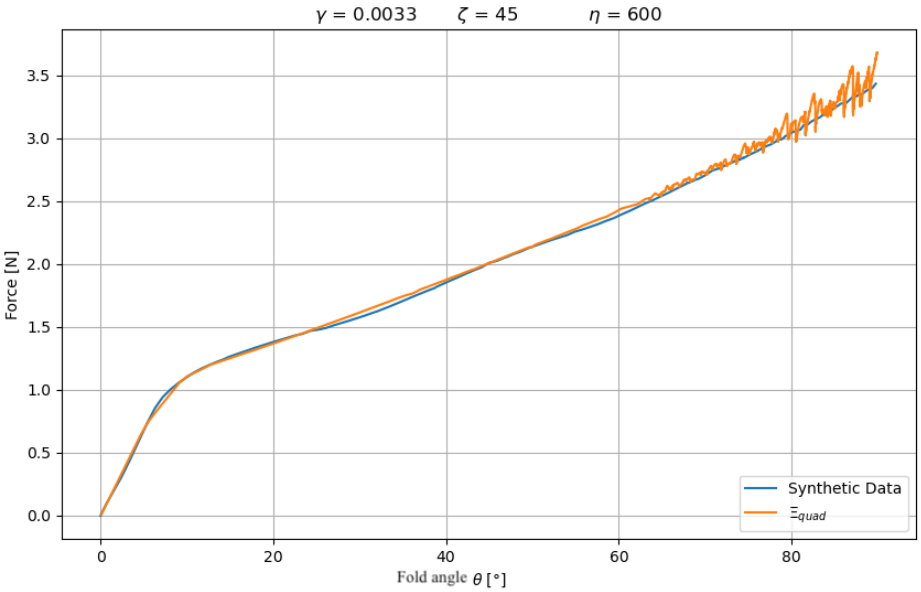

Figure 35: Quadratic type hardening behavior assumed

Figure 35 represents a seemingly good fit, concluding the characterization of the elasto-plastic beam model for a simple $[0, 90]$ fold of a crease. There also appears to be some correlation between the shape of the function defining the hardening curve and the shape of the response curve during yielding, which could prove to be useful as data more representative of crease folding becomes available.

5.3 Offloading and Influence of Hardening Mode

Figure 36 show force - rotation curves for fold cycle $[0, 90, -90]$ for values μ of 0, 0.5 and 0.99, along with the synthetic data curve.

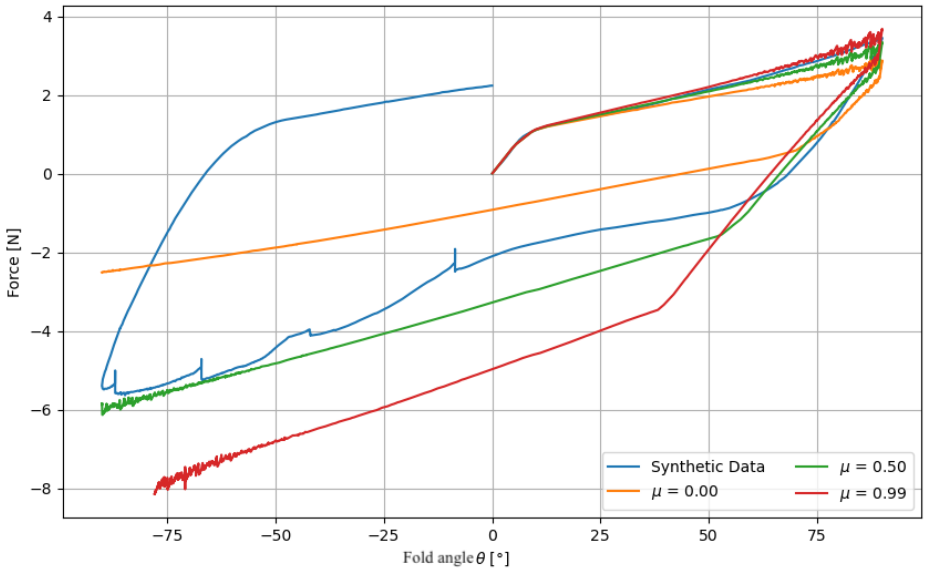

Figure 36: Isotropic-, kinematic- and combined hardening

Figure 36 illustrates how μ can be calibrated in order to achieve the mix of hardening modes that is needed, though the introduction of the combined mode of hardening also introduces some unexplained artifacts in the modeling, the three choices of μ result in three slightly different curves of differing slopes during yielding in the first fold from 0 to 90 degrees. The reason for this behavior is at the moment unknown to the author. In the offloading none of the curves are able to capture the hardening of the board as the fold goes from a natural mode to counter-type fold, the consequences of this being illustrated in Figure 37:

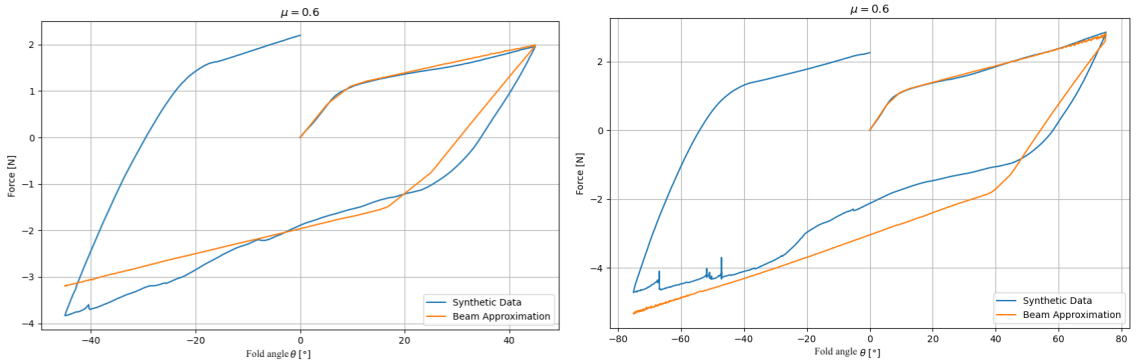

(a) 45° (b) 75°

Figure 37: Same combined hardening parameters for different angles used in fold cycle

It can be observed that different fold cycle angles result in the beam-approximation over- or underestimating the response in the offloading/counter folding part of the cycle, given that the same μ is used. This necessitates calibration dependent on the known specific fold sequence that is to be studied. Finally Figure 38 further shows how the calibration of the hardening mode influences the response, now in the final part of the fold cycle:

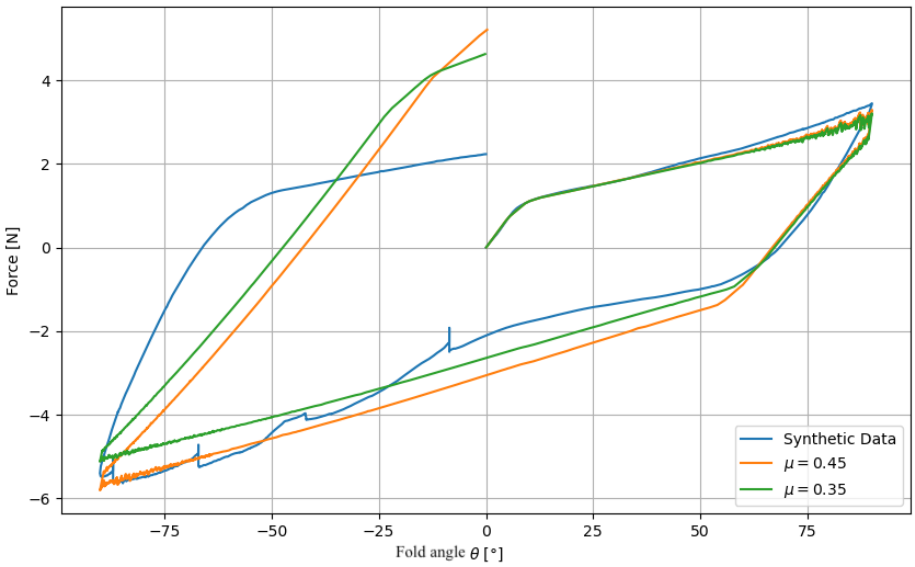

Figure 38: Full fold cycle using $\mu = 0.45$ and $\mu = 0.35$

Both approximation curves fail to capture the synthetic data response, both showing comparatively less stiffness in the initial part of the final -90 to 0 degree fold of the sequence. The elastic regime of response is also overestimated compared to the synthetic data, since it can observed around -30 degrees that the beam curves retain their linear elastic response while the synthetic curve slope indicates that the crease has yielded.

6 Conclusion

The proposed beam model which utilizes relatively simple tools already built into Abaqus was able to capture the macroscopic behavior defined by the synthetic data with reasonable accuracy. The response of the initial fold is relatively easy to capture by reducing the area moment of inertia of a beam and a simple isotropic hardening behavior for the plastic yielding. The response behavior of the return fold is generally captured by a combination of kinematic and isotropic hardening, though calibration of the response has to be done based on the nature of the predetermined fold sequence (see Figure 37). The final fold back to 0 degrees is deemed as the hardest part of the response to capture, and no simple modeling tools available in Abaqus are likely to solve the issue. The modeling method could possibly be applied for simpler folding applications, such as fold sequences that don't constitute a full cycle, which is typically not the case in package forming.

7 Future Work

Though the modeling approach presented in this thesis was partly successful for capturing the synthetic data that was produced, there are still a plethora of considerations that will have to be taken into account if the model is to be used in future endeavors. First, the model should ideally be calibrated against real experimental data of creased paperboard folding, which as previously stated doesn't currently exist for the more complex fold cycles that have been studied in the work. Alternatively the Robertsson model could be used in order to create the synthetic data that is to be modeled after.

Apart from the specifics of calibration and what data to calibrate against, there are multiple potential issues that have been identified and may require more work to solve before using the model in converting simulations. For instance, the bending moment and normal force of a beam are both directly coupled to the normal stress σ_{xx}. Effort was spent decoupling the beam response in these modes by the introduction of α and β, which might suffice when the stress state of the beam integration points are within the elastic regime of loading, but the plastic onset of an integration point has no mechanism that differentiates the mode of loading, which might prove problematic. Ideally further separation of the bending- and monotonic axial- loading modes could be done by so-called double stacking of specialized beam elements, one that only responds to bending and one that only responds to tension/compression respectively. Alternatively the response of the integration points could be coupled by some form of macro-function within a UMAT-routine that determines the response as a function of the general stress state.

Entering the third spacial dimension is eventually necessary since that is how converting simulations are performed, however the modeling complexity is increased by having to take into consideration an additional mode of bending, which will also be dependent on σ_{xx} throughout the cross-sectional width instead of the height. The extent to which this could be an issue is unknown until tested.

Finally the use of a beam also disregards the influence of any forces acting through the crease line, i.e there are no stresses σ_{yy}. The resulting reduction in stiffness regarding the full paperboard in that regard might be negligible, due to the crease are being relatively small compared to the size of the full board, but this could be included by modeling the crease zone as shell elements, though it would have to be done with the use of a user defined element. An added benefit of a shell implementation would be that the process of meshing the crease domain would be simplified, since adding beam elements would have to be done manually for each node otherwise.

References

[1] Tetra Pak, "Tetra Pak Solutions: Packaging Materials," 2024. Accessed: 2024-03-26.

[2] L. Beex and R. Peerlings, "An experimental and computational study of laminated paperboard creasing and folding," *International Journal of Solids and Structures*, vol. 46, no. 24, pp. 4192–4207, 2009.

[3] D. Coffin and M. Nygårds, "Creasing and folding," in *Advances in Pulp and Paper Research, Oxford 2017, Trans. of the XVIth Fund. Res. Symp. Oxford* (W. Batchelor and D. Söderberg, eds.), pp. 69–136, FRC, Manchester, 2018.

[4] N. Stenberg and C. Fellers, "Out-of-plane poisson's ratios of paper and paperboard," *Nordic Pulp & Paper Research Journal*, vol. 17, no. 4, pp. 387–394, 2002.

[5] S. Nagasawa, Y. Fukuzawa, T. Yamaguchi, S. Tsukatani, and I. Katayama, "Effect of crease depth and crease deviation on folding deformation characteristics of coated paperboard," *Journal of Materials Processing Technology*, vol. 140, no. 1, pp. 157–162, 2003. Proceedings of the 6th Asia Pacific Conference on materials Processing.

[6] A. N. Giampieri, *An Interface Element To Model The Mechanical Response Of Crease Lines For Carton-Based Packaging*. Phd. thesis, Politecnico Di Milano. Dept. of Structural Engineering, Mar. 2009.

[7] Q. Xia, *Mechanics of inelastic deformation and delamination in paperboard*. Phd. thesis, Massachusetts Institute of Technology. Dept. of Mechanical Engineering, Jan. 2002.

[8] E. Borgqvist, T. Lindström, J. Tryding, M. Wallin, and M. Ristinmaa, "Distortional hardening plasticity model for paperboard," *International Journal of Solids and Structures*, vol. 51, no. 13, pp. 2411–2423, 2014.

[9] E. Borgqvist, M. Wallin, M. Ristinmaa, and J. Tryding, "An anisotropic in-plane and out-of-plane elasto-plastic continuum model for paperboard," *Composite Structures*, vol. 126, pp. 184–195, 2015.

[10] K. Robertsson, E. Jacobsson, M. Wallin, E. Borgqvist, M. Ristinmaa, and J. Tryding, "A continuum damage model for creasing and folding of paperboard," *Packaging Technology and Science*, vol. 36, no. 12, pp. 1037–1050, 2023.

[11] L. Buldgen, H. Le Sourne, N. Besnard, and P. Rigo, "Extension of the super-elements method to the analysis of oblique collision between two ships," *Marine Structures*, vol. 29, no. 1, pp. 22–57, 2012.

[12] H.-S. Kim and D.-G. Lee, "Analysis of shear wall with openings using super elements," *Engineering Structures*, vol. 25, no. 8, pp. 981–991, 2003.

[13] R. Pecora, M. Magnifico, F. Amoroso, L. Lecce, M. Bellucci, I. Dimino, A. Concilio, and M. Ciminello, "Structural design of an adaptive wing trailing edge for large aeroplanes," in *Smart Intelligent Aircraft Structures (SARISTU)* (P. C. Wölcken and M. Papadopoulos, eds.), (Cham), pp. 159–170, Springer International Publishing, 2016.

[14] P. Mäkelä and S. Östlund, "Orthotropic elastic–plastic material model for paper materials," *International Journal of Solids and Structures*, vol. 40, no. 21, pp. 5599–5620, 2003.

[15] A. Karafillis and M. Boyce, "A general anisotropic yield criterion using bounds and a transformation weighting tensor," *Journal of the Mechanics and Physics of Solids*, vol. 41, no. 12, pp. 1859–1886, 1993.

[16] A. Harrysson and M. Ristinmaa, "Large strain elasto-plastic model of paper and corrugated board," *International Journal of Solids and Structures*, vol. 45, no. 11, pp. 3334–3352, 2008.

[17] N. Stenberg, "A model for the through-thickness elastic-plastic behaviour of paper," *International Journal of Solids and Structures*, vol. 40, no. 26, pp. 7483–7498, 2003.

[18] L. Beldie, *Mechanics of Paperboard Packages - Performance at Short Term Static Loading*. Licentiate thesis, Lund University (LTH), Lund, Sweden, Oct. 2001.

[19] P. Zhao, J. Liu, C. Wu, S. Ye, Q. Yang, and G. Hao, "Deployment analysis of membranes with creases using a nonlinear torsion spring model," *International Journal of Mechanical Sciences*, vol. 255, p. 108444, 2023.

[20] M. Schenk, S. D. Guest, *et al.*, "Origami folding: A structural engineering approach," *Origami*, vol. 5, pp. 291–304, 2011.

[21] S. R. Woodruff and E. T. Filipov, "A bar and hinge model formulation for structural analysis of curved-crease origami," *International Journal of Solids and Structures*, vol. 204-205, pp. 114–127, 2020.

[22] Dassault Systèmes, *Dassault Systèmes Abaqus User Manual*, 2024.

[23] N. Ottosen and M. Ristinmaa, *The mechanics of constitutive modeling*, ch. 4. Elsevier, 1 ed., 2005.